Nanoscale

PAPER

View Article Online
View Journal | View Issue

Check for updates

Cite this: *Nanoscale*, 2019, **11**, 4999

In situ TEM study on diversified martensitic transition behaviour in $Ni_{50}Mn_{35}In_{15}$ alloys

Shulan Zuo,[a,b,c] Yao Liu,[a,b] Ying Zhang,*[a,c] Jiefu Xiong,[a,b] Jun Liu,[a,b] Kaiming Qiao,[a,b] Feixiang Liang,[a,b] Tongyun Zhao,[a,c] Fengxia Hu,[a,b] Jirong Sun[a,b] and Baogen Shen*[a,b]

Received 18th December 2018,
Accepted 19th February 2019

DOI: 10.1039/c8nr10209k

rsc.li/nanoscale

Ni–Mn–In magnetic shape-memory alloys are attractive materials due to their important functional properties relating to the martensitic transition. Understanding the complex martensitic magnetism and the transition process is of crucial importance not only from a fundamental but also from a technological point of view. Here, we demonstrate the dynamic magnetic domains and microstructures during the martensitic transition in the bulk and melt-spun ribbons of $Ni_{50}Mn_{35}In_{15}$ *via in situ* Lorentz transmission electron microscopy. The significant evolutionary differences in correlation with the temperature dependence of magnetization are identified between the bulk and ribbons. For a bulk alloy with $L2_1$ crystal structure at room temperature, the complete martensite with 7 M modulation in the paramagnetic state and the successive stripe magnetic domains in ferromagnetic martensite develop with a further decrease in the temperature. The stripe domains evolve into biskyrmion-like spin configurations when a perpendicular magnetic field is applied. In contrast, the partial austenitic phase always coexists with the martensitic phase in the ribbons even far below the martensitic transition temperatures and the martensitic phase presents a dominant twinning stack morphology with 5 M modulation and various magnetic domains. During the subsequent reheating-cooling cycles, the thermal hysteresis behavior and the transition reversibility in the bulk and ribbons are represented *via* the microstructural evolution.

1. Introduction

Ni-based Heusler alloys have attracted significant interest due to their rich physical properties and applications as ferromagnetic shape memory alloys (FSMAs) and magnetocaloric materials.[1–13] Most FSMAs exhibit a structural transformation from the parent austenite to the martensitic phase upon cooling, with an abrupt magnetization change. The diffusionless and solid-to-solid martensitic phase transformations contribute to the structural changes with the symmetry reduction giving rise to the formation of ferroelastic domains, *i.e.* twin variants.[7,8] The coupling between magnetic domains and the twin variants *via* magnetocrystalline anisotropy[9] contributes to the corresponding mechanical,[10] electromagnetic,[1,11,12] and transport properties[13] suitable for practical applications.

The strong magnetoelastic coupling with a large magnetization difference between the ferromagnetic austenite and martensite with a change in temperature changes the transition temperatures considerably when magnetic fields are applied in Ni–Mn–In Heusler alloys. Therefore, Ni–Mn–In alloys are identified as good candidates to take advantage of the magnetic field/temperature-induced phase transition. The magnetization changes rapidly over a narrow temperature range near the martensitic transition with the coexistence of austenitic and martensitic phase, which gives rise to complex magnetic exchange. Understanding the unique magnetic and structural evolution accompanying the martensitic transition of Ni–Mn–In alloys is of great importance for their application and material exploration.

Significant experiments and theories have been devoted to studying the magnetic correlations during martensitic transformations.[14–18] Polarized neutron diffraction studies on $Ni_{50}Mn_{37}Sn_{13}$ and $Ni_{50}Mn_{40}Sb_{10}$ have verified the presence of complex antiferromagnetic correlations in this transition.[15] The existence of ferromagnetic and antiferromagnetic coupling was identified in $Ni_{49.1}Mn_{35.4}In_{15.5}$ and $Ni_{49.9}Mn_{37}Sn_{13.1}$ by a ferromagnetic resonance technique,[17] whereas the martensitic phase in the $Ni_{50}Mn_{34.8}In_{15.2}$ alloy was determined to be paramagnetic by Mössbauer spectroscopy.[18] Various domain structures inside a martensitic twin variant due to the relative orientation difference of the magnetic easy axis were

[a]*State Key Laboratory of Magnetism, Institute of Physics, Chinese Academy of Sciences, Beijing 100190, P. R. China. E-mail: shenbg@iphy.ac.cn, zhangy@iphy.ac.cn*
[b]*University of Chinese Academy of Sciences, Beijing, 100049, P. R. China*
[c]*Fujian Institute of Innovation, Chinese Academy of Sciences, Fuzhou, Fujian 350108, P. R. China*

confirmed through dependency on external magnetic fields.[19] Therefore, the magnetic nature of the martensitic phase still remains diverse and elusive so far. Most studies on Ni–Mn–In alloys have focused on the structure, magnetic properties,[20–23] substitution effects and order-disorder transformation from the macro point-of-view.[24,25] Few systematic studies have been reported on direct observation of the evolution of the magnetic domains during phase transformation, and this will be explored here during the martensitic transition in $Ni_{50}Mn_{35}In_{15}$ bulk and ribbons *via in situ* Lorentz transmission electron microscopy (LTEM). The significant evolutionary differences in magnetic domains and microstructures of the bulk and melt-spun ribbons of $Ni_{50}Mn_{35}In_{15}$ alloy are revealed during the transition between the parent austenite and the martensitic phase.

2. Experimental

A polycrystalline $Ni_{50}Mn_{35}In_{15}$ ingot is synthesized by using an arc melting technique in a high-purity argon atmosphere, and the polycrystalline ribbons are obtained by using a single-roller melt spinning method with wheel surface velocities of 15 and 30 m s^{-1}, here named R15 and R30 respectively. The details of the material preparation and other physical properties will be reported elsewhere. Thin plates for LTEM observation were individually cut from the bulk and ribbons, and then thinned by traditional mechanical polishing and argon ion milling. To image the crystal microstructure and magnetic domain configuration, a JEOL-dedicated LTEM is used with almost no remnant magnetic field near the sample. *In situ* cooling experiments are conducted using a liquid-nitrogen TEM sample holder (100–300 K). The thermal effects of the transmission electron beam play a minor role in the *in situ* cooling phase transition of Ni–Mn–In alloys. Magnetic domain walls are imaged as bright or dark contrast on the defocused image planes due to electron deflection in the Fresnel Lorentz TEM mode. Quantitative in-plane magnetization maps are obtained based on the defocused Fresnel LTEM images *via* the transport-of-intensity equation (TIE). The magnetic properties are measured by a superconducting quantum interference magnetometer (SQUID-VSM). The crystal structures of the samples are checked by x-ray powder diffraction equipped with Cu–K radiation.

3. Results and discussion

3.1 Martensitic transformation in $Ni_{50}Mn_{35}In_{15}$ alloys

The temperature dependence of magnetization (M–T curves) in an external field of 10 mT is measured in $Ni_{50}Mn_{35}In_{15}$ alloys in the form of bulk and ribbons, as shown in Fig. 1. Abrupt magnetization peaks correlated with the change in magnetization of the M–T curve are observed when the temperature is decreased. The martensitic transition temperature (T_M) is defined at the largest positive slope of the cooling M–T curve

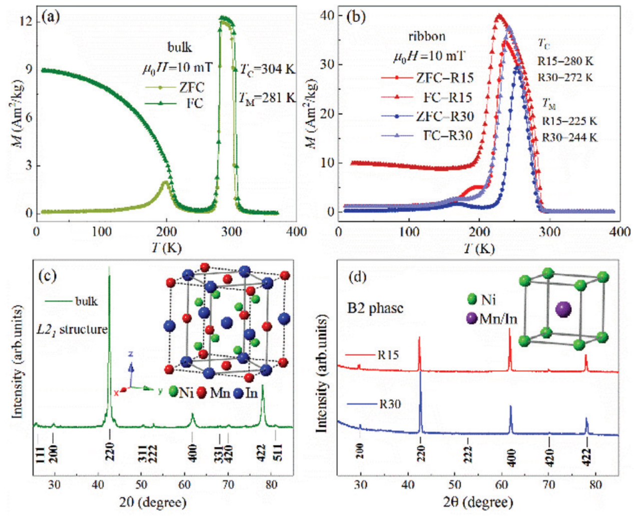

Fig. 1 Temperature dependency of magnetization (M–T curves) measured at a magnetic field of 10 mT for the $Ni_{50}Mn_{35}In_{15}$ alloy in the form of (a) bulk and (b) ribbons. The X-ray diffraction patterns for $Ni_{50}Mn_{35}In_{15}$ alloy in the form of (c) bulk and (d) ribbons at room temperature. The insets show the schematic cubic $L2_1$ and B2 structures of parent austenite for the bulk and ribbon respectively.

and thus T_M and the ferromagnetic Curie temperature (T_C) are identified to be about T_C = 304 K, T_M = 281 K for bulk, in contrast to T_C = 280 K, T_M = 225 K and T_C = 272 K, T_M = 244 K for the melt-spun ribbons R15 and R30 respectively. Overall, the phase transition temperature is a little bit higher in the bulk than in the ribbons due to the larger grain size. The two separate peaks in the bulk merged into one broader peak in the ribbons. The large magnetization splitting between zero field-cooling (ZFC) and field-cooling (FC) at a low temperature below the martensitic transition may result from the spin reorientation to ferromagnetic components under external magnetic fields in both the bulk and ribbons[26,27] which are associated with the pinning from the coexisting antiferromagnetic exchange, or noncollinear magnetic structures residing within the twin boundaries in the martensitic phase.[20] The XRD at room temperature demonstrates the $L2_1$ crystal structure (Fig. 1c) for the bulk alloy and a partially ordered phase (B2) in the ribbons (Fig. 1d). The significant changes in magnetization of the bulk and ribbons in Fig. 1 may result from different structures and grain sizes.

3.2 Magnetic domain and crystal structure in $Ni_{50}Mn_{35}In_{15}$ bulk alloy

To understand the significant changes in magnetization in the above M–T curves, the phase transformation behaviour is directly observed using LTEM while altering the temperatures in the $Ni_{50}Mn_{35}In_{15}$ alloy. The magnetic domain evolution of bulk $Ni_{50}Mn_{35}In_{15}$ alloy as it cools from 293 to 115 K is demonstrated in the under-focused Lorentz TEM images, as shown in Fig. 2. The selected area diffraction (SAED) patterns along the [110] zone-axis (the inset of Fig. 2a) and x-ray diffraction (not shown here) confirm the $L2_1$ crystal structure of the austenitic

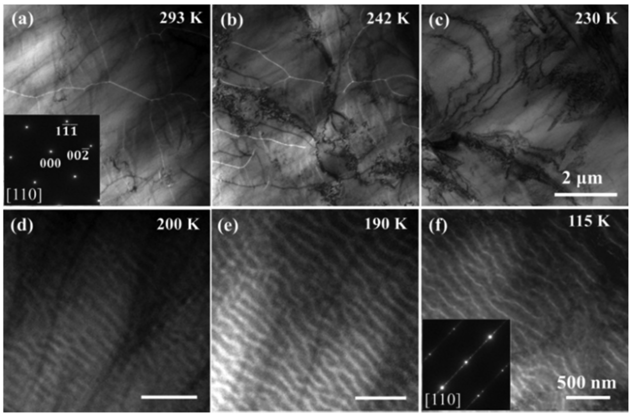

Fig. 2 Under-focused LTEM images of temperature-induced magnetic domain evolution during cooling in the bulk $Ni_{50}Mn_{35}In_{15}$ alloy. The insets show the selected area electron diffraction (SAED) indicating the [110] zone axis. The scale bar in (d)–(f) is 500 nm.

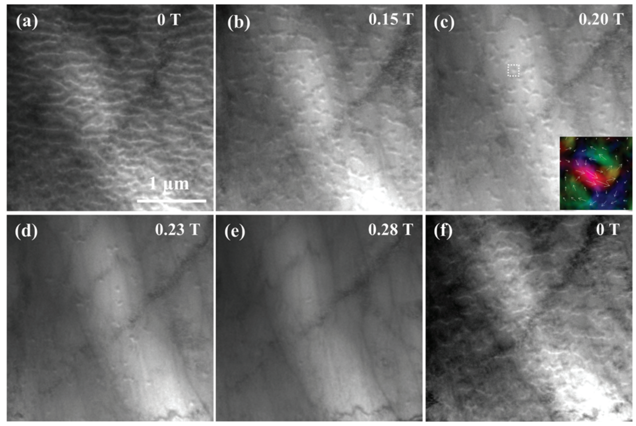

Fig. 3 The magnetic field dependency of domain evolution in the martensitic phase of bulk alloy at 150 K. Under-focused LTEM images with an increase in the magnetic field from (a) 0 T, to (b) 0.15 T, (c) 0.20 T, (d) 0.23 T and (e) 0.28 T. (f) The residual state after switching off the magnetic field. The inset shows the corresponding in-plane magnetization distribution obtained *via* TIE for the selected area of (c).

phase. The irregularly large magnetic domains at 293 K (Fig. 2a) become narrower when the temperature is decreased to 242 K (below T_M = 280 K), as shown in Fig. 2b. As the temperature is decreased to 230 K, the disappearance of the magnetic domain wall contrast (Fig. 2c) implies a complete martensitic phase transition into a paramagnetic state, which corresponds well with the dropped platform in the M–T curves of both ZFC and FC and with previous reports.[15,18] When the temperature is decreased further to 200 K, the paramagnetic-ferromagnetic transformation of the martensitic phase[15] is represented as spontaneous stripe-like magnetic domains (Fig. 2d), which is further identified as a helical magnetic structure. The magnetic domain contrast is enhanced (Fig. 2e) and the magnetic domains become wider at 115 K (Fig. 2f) as the temperature decreases. The magnetic domains at different temperatures upon heating (from 115 to 293 K) are similar to those in the cooling process, presenting a reversible phase transformation, in good correlation with the little heat hysteresis of the M–T curve.

The magnetization distribution of the above stripe-like magnetic domains is further unveiled through the magnetic field dependency of the magnetic domain evolution at 150 K, as demonstrated in Fig. 3. The under-focused LTEM images (Fig. 3a–e) show that the magnetic stripes evolve into individual biskyrmion-like nanodomains with an increase in the magnetic field. At zero magnetic field, there are a series of magnetic stripes with an averaged period of about 100 nm. As the magnetic field is increased, the magnetic stripes first become narrow, and then break into round-shaped domains. The biskyrmion-like domains are observed at a magnetic field of about 0.2 T (Fig. 3c). The nanodomains start to disappear and then completely vanish into a saturated ferromagnetic state at a magnetic field above 0.28 T. Similar stripe domains reappear in the residual state (Fig. 3f) after the magnetic field has been reduced back to zero. The magnetic field-dependent behaviour of the stripe domains is similar to the classic stripe-to-skyrmion evolution in previous studies,[28–30] which indicates the canted magnetization distribution in the stripes during the magnetic transition.

3.3 Diversiform martensitic transformation and magnetic domains in R15 $Ni_{50}Mn_{35}In_{15}$ ribbons

Considering the significant differences in M–T curves between the bulk and ribbons of $Ni_{50}Mn_{35}In_{15}$, the martensitic transformation behaviour in the R15 ribbons is further studied using LTEM. Unlike the irregular magnetic domains in the bulk alloy (Fig. 2a), the paramagnetic-ferromagnetic transition of the austenite phase results in the presence of parallel 180° domains at a temperature below T_C ~ 280 K, as shown in Fig. 4a and b. The transformation from the austenite to the martensitic phase with a further decrease in temperature is presented by the partial disappearance of the 180° magnetic domains and the appearance of acicular martensitic configur-

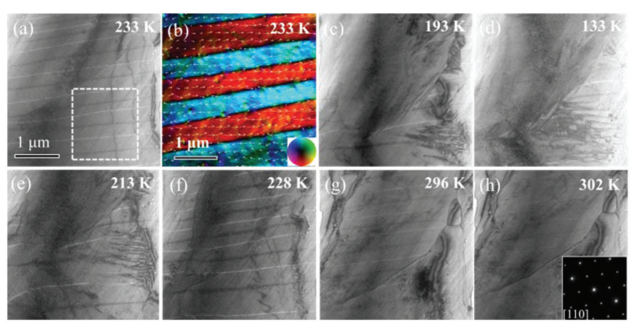

Fig. 4 The temperature dependency of the microstructure and magnetic domain evolution in the R15 ribbon. Under-focused LTEM images of (a) spontaneous 180° domains in austenite phase at 233 K and (b) corresponding in-plane magnetization obtained by TIE for the selected areas. Magnetic domain morphologies when cooled to (c) 193 K, (d) 133 K, and reheated to (e) 213 K, (f) 228 K, (g) 296 K and (h) 302 K. The insets of (h) show the (SAED) along the [110] zone axis.

ations with a dark contrast (Fig. 4c and d). The complete paramagnetic martensite as in the bulk alloy (Fig. 2c) is not observed here, which corresponds with the magnetization change in the *M*–*T* curves. It is also notable that the ferromagnetic austenite always coexists with martensite in the ribbon, even though the temperature is decreased lower than 120 K (far below the martensitic transition $T_M \sim 225$ K), suggesting that the martensitic transition is kinetically arrested[31–35] without obtaining the fully complete martensite. The partially ordered B2 structure in the melt-spun ribbons identified *via* x-ray diffraction (Fig. 1d) in contrast to the fully-ordered $L2_1$ austenite contributes to the significant differences in structure and magnetization between the bulk and ribbons. The hysteresis behavior in correlation with the *M*–*T* curves (Fig. 1b) is demonstrated with higher temperatures for the existence of the martensitic phase during the heating than that for the cooling. The acicular martensitic structures diminish and the 180° domains reappear across the martensite to austenite transition, as shown in Fig. 4e and f. The diminishing of the magnetic domain contrast near T_C = 280 K (Fig. 4g–h) correlates with the ferromagnetic-paramagnetic transition of the austenite phase under heating.

The martensitic phase transition is usually complicated by the appearance of different morphologies.[36,37] Besides the acicular martensitic configurations in Fig. 4, some grains are filled with twinning plates (Fig. 5a) with rows of bright or dark dot (vortex-like) domains within the variants where the easy axis should be out-of-plane.[38] Magnetic domain evolution by altering the temperature is demonstrated in the under-focused LTEM images (Fig. 5a–g). The SAED at 122 K indicates a 5 M modulation twinning structure along the [001] zone axis in this martensitic grain. As the temperature is increased to 172 K (Fig. 5b), the morphology configuration does not change much. The martensitic twinning plates totally disappear above 250 K (Fig. 5c), indicating that the crystal structure of the martensitic phase has been completely changed. The observed maze-like magnetic domains result from the magnetic phase transition.[19,39] No magnetic contrast is observed when the temperature is higher than T_C (Fig. 5d). A subsequent cooling experiment is conducted to reveal the reversibility of the martensitic transformation in connection with thermal hysteresis behaviour, as shown in Fig. 5e–g. When the temperature is decreased to 227 K (close to $T_M \sim 225$ K), the martensitic twinning structure grows from the parent austenite (Fig. 5e). More martensitic twinning features appear when the temperature is decreased to 152 K (Fig. 5f). Accompanying the change in crystal structure, a nearly zigzag magnetic domain wall (indicated by the red arrow) resides across the twinning structure.[9] The martensitic twinning structure occupies almost the whole grain at 122 K (Fig. 5g), with the enlarged areas A and B shown in Fig. 5h and i, demonstrating the nearly-complete martensitic structure. The diffraction pattern in SAED (the inset of Fig. 5g) indicates different modulation structures in comparison with the initial one (Fig. 5a) and the heating–cooling cycle is irreversible. Therefore, it is clearly demonstrated that the crystal structure and magnetic domains interact with each other during the martensitic transition by correlating the twinning structure with the magnetic anisotropy.[19]

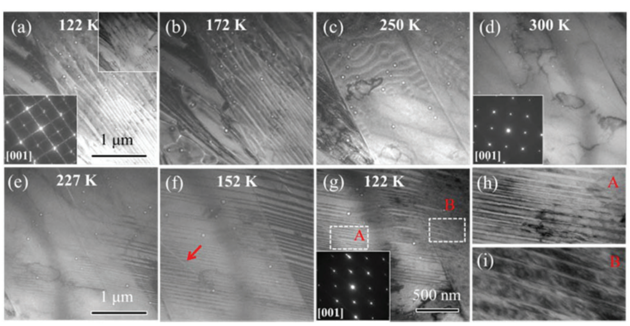

Fig. 5 The temperature dependency of diversified microstructural evolution in R15 ribbons. Under-focused LTEM images of magnetic domains at (a) 122 K, (b) 172 K, (c) 250 K, and (d) 300 K during heating and (e) 227 K, (f) 152 K, (g) 122 K during recooling. (h, i) The enlarged bright field images from the selected area of (g). The corresponding bright field TEM image at the right corner of the inset of (a). The SAED (insets at left corner) along the [001] zone axis presenting 5 M modulation in the martensitic phase.

3.4 Reversibility of martensitic transformation in R30 $Ni_{50}Mn_{35}In_{15}$ ribbons

The significant difference in the *M*–*T* curves between the bulk and the R15 ribbon has been revealed in the above phase transition *via* direct *in situ* LTEM images. The effects of the different wheel speeds used for preparing the sample on the martensitic transition are further studied. The twinning crystal structures and vortex-like domains (the inset of Fig. 6a) are observed in the martensitic phase. Vortex-like noncollinear magnetic structures residing within the twinning boundaries have been found in both R15 and R30 ribbons. Microstructural evolution upon two cooling cycles in the R30 ribbon are shown in Fig. 6, with no obvious changes in the martensitic morphology (Fig. 6a and c). The different reversal behaviors between R15 and R30 in response to the thermal cycles correlate with the magnetization splitting degree of their *M*–*T* curves between ZFC and FC at low temperature. The ribbons with different wheel speeds have different atomic orders and grain

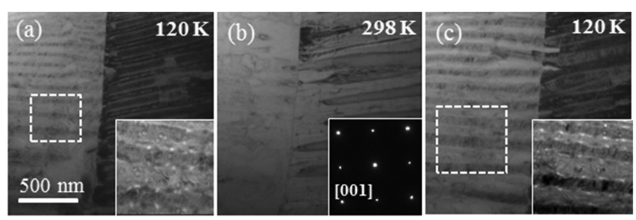

Fig. 6 Microstructural evolution during the thermal cycles between 298 and 120 K in the R30 ribbons. The bright field images taken (a) at 120 K in the first cooling, (b) first heating back to 298 K, and (c) second cooling to 120 K. The under-focused LTEM images of the selected areas are given in insets, indicating the appearance of vortex-like domains. The insets of (b) show the (SAED) indicating the [001] zone axis.

sizes, which may affect the martensitic phase transformation and lead to the anomalous behavior mentioned above.[36,40]

4. Conclusions

In summary, the martensitic transitions in the presence of various morphologies of both crystal structures and magnetic domains are systematically studied with a significant difference between the bulk and ribbons of $Ni_{50}Mn_{35}In_{15}$ alloys *via in situ* LTEM. During the cooling process of bulk $Ni_{50}Mn_{35}In_{15}$, martensite in the paramagnetic state is observed and the uniform stripe-like magnetic domains in the form of a canted magnetization distribution subsequently develop at a lower temperature. The parallel 180° magnetic domains in the ribbon are observed to be different from the irregular large magnetic domain of the austenite phase in the bulk material. The thermal hysteresis behavior and the transition reversibility in response to the heating–cooling cycles are demonstrated *via* the microstructural evolution in the bulk and ribbons, which are consistent with the *M–T* curves. The crystal structure and magnetic domains interact with each other and introduce various martensitic morphologies below T_M. The dramatic change in magnetic domain structure between the bulk and ribbons is closely related to the degree of atomic order, with an $L2_1$ structure for the bulk alloy and B2 for the ribbons. The various magnetic domain evolutions indicate that the martensitic phase has different magnetic states. The effect of thermal cycling on the martensitic structure depends on the preparation conditions of the sample, which influence the reversibility of the martensitic transition. The discovery of diversified magnetic transitions and noncollinear magnetic structures will help us to explore martensitic properties and the fundamental physics of topologically nontrivial spin textures.

Author contributions

Baogen Shen, Ying Zhang conceived and designed the experiments. Shulan Zuo performed the experiments. Yao Liu synthesized the samples. Jun Liu contributed to the LTEM experiments. Jiefu Xiong, Kaiming Qiao, and Feixiang Liang contributed to magnetization measurements. Tongyun Zhao, Fengxia Hu, Jirong Sun, and Baogen Shen contributed to the result analysis. Shulan Zuo, Ying Zhang and Baogen Shen analyzed the data and wrote the manuscript. All authors discussed the results and commented on the manuscript.

Conflicts of interest

There are no conflicts to declare.

Acknowledgements

This work was supported by the National Key Research and Development Program of China (Grant No. 2017YFA0206300, 2016YFA0300701, 2016YFB0700903, 2014CB643702), the National Natural Sciences Foundation of China (Grant No. 51590880, 11874408, 51431009, 11520101002), the Key Research Program of the Chinese Academy of Sciences of China, and the Youth Innovation Promotion Association, CAS, 2015004.

References

1 J. Liu, T. Gottschall, K. P. Skokov, J. D. Moore and O. Gutfleisch, *Nat. Mater.*, 2012, **11**, 620–626.
2 R. Kainuma, Y. Imano, W. Ito, Y. Sutou, H. Morito, S. Okamoto, O. Kitakami, K. Oikawa, A. Fujita, T. Kanomata and K. Ishida, *Nature*, 2006, **439**, 957–960.
3 H. E. Karaca, I. Karaman, B. Basaran, Y. Ren, Y. I. Chumlyakov and H. J. Maier, *Adv. Funct. Mater.*, 2009, **19**, 983–998.
4 B. M. Wang, Y. Liu, P. Ren, B. Xia, K. B. Ruan, J. B. Yi, J. Ding, X. G. Li and L. Wang, *Phys. Rev. Lett.*, 2011, **106**, 077203.
5 I. Dubenko, A. K. Pathak, S. Stadler, N. Ali, Y. Kovarskii, V. N. Prudnikov, N. S. Perov and A. B. Granovsky, *Phys. Rev. B: Condens. Matter Mater. Phys.*, 2009, **80**, 092408.
6 V. K. Sharma, M. K. Chattopadhyay, K. H. B. Shaeb, A. Chouhan and S. B. Roy, *Appl. Phys. Lett.*, 2006, **89**, 222509.
7 M. Pitteri and G. Zanzotto, *Continuum Models for Phase Transitions and Twinning in Crystals*, CRC Press, 2002.
8 K. Bhattacharya, *Microstructure of Martensite: Why it Forms and how it Gives Rise to the Shape-memory Effect*, OUP Oxford, 2003.
9 A. Budruk, C. Phatak, A. K. Petford-Long and M. De Graef, *Acta Mater.*, 2011, **59**, 6646–6657.
10 C. Bechtold, C. Chluba, R. Lima de Miranda and E. Quandt, *Appl. Phys. Lett.*, 2012, **101**, 091903.
11 X. Moya, E. Stern-Taulats, S. Crossley, D. Gonzalez-Alonso, S. Kar-Narayan, A. Planes, L. Manosa and N. D. Mathur, *Adv. Mater.*, 2013, **25**, 1360–1365.
12 V. Srivastava, X. Chen and R. D. James, *Appl. Phys. Lett.*, 2010, **97**, 014101.
13 N. F. Mott and L. Friedman, *Philos. Mag.*, 2006, **30**, 389–402.
14 P. Bhobe, K. Priolkar and A. Nigam, *J. Phys. D: Appl. Phys.*, 2008, **41**, 235006.
15 S. Aksoy, M. Acet, P. P. Deen, L. Mañosa and A. Planes, *Phys. Rev. B: Condens. Matter Mater. Phys.*, 2009, **79**, 212401.
16 C. L. Tan, Y. W. Huang, X. H. Tian, J. X. Jiang and W. Cai, *Appl. Phys. Lett.*, 2012, **100**, 132402.
17 S. Aksoy, O. Posth, M. Acet, R. Mackenstock, J. Lindner, M. Farle and E. F. Wassermann, *J. Phys.: Conf. Ser.*, 2010, **200**, 092001.
18 R. Y. Umetsu, R. Kainuma, Y. Amako, Y. Taniguchi, T. Kanomata, K. Fukushima, A. Fujita, K. Oikawa and K. Ishida, *Appl. Phys. Lett.*, 2008, **93**, 042509.
19 A. Budruk, C. Phatak, A. K. Petford-Long and M. De Graef, *Acta Mater.*, 2011, **59**, 4895–4906.

20 T. Krenke, M. Acet, E. F. Wassermann, X. Moya, L. Mañosa and A. Planes, *Phys. Rev. B: Condens. Matter Mater. Phys.*, 2006, **73**, 174413.
21 A. K. Pathak, M. Khan, I. Dubenko, S. Stadler and N. Ali, *Appl. Phys. Lett.*, 2007, **90**, 262504.
22 M. K. Chattopadhyay, M. A. Manekar, V. K. Sharma, P. Arora, P. Tiwari, M. K. Tiwari and S. B. Roy, *J. Appl. Phys.*, 2010, **108**, 073909.
23 T. Krenke, S. Aksoy, E. Duman, M. Acet, X. Moya, L. Mañosa and A. Planes, *J. Appl. Phys.*, 2010, **108**, 043914.
24 Z. H. Liu, S. Aksoy and M. Acet, *J. Appl. Phys.*, 2009, **105**, 033913.
25 T. Miyamoto, W. Ito, R. Y. Umetsu, R. Kainuma, T. Kanomata and K. Ishida, *Scr. Mater.*, 2010, **62**, 151–154.
26 E. Duman, M. Acet, Y. Elerman, A. Elmali and E. F. Wassermann, *J. Magn. Magn. Mater.*, 2002, **238**, 11.
27 E. Duman, M. Acet, I. Dincer, A. Elmali and Y. Elerman, *J. Magn. Magn. Mater.*, 2007, **309**, 40–53.
28 X. Z. Yu, Y. Tokunaga, Y. Kaneko, W. Z. Zhang, K. Kimoto, Y. Matsui, Y. Taguchi and Y. Tokura, *Nat. Commun.*, 2014, **5**, 3198.
29 W. Wang, Y. Zhang, G. Xu, L. Peng, B. Ding, Y. Wang, Z. Hou, X. Zhang, X. Li, E. Liu, S. Wang, J. Cai, F. Wang, J. Li, F. Hu, G. Wu, B. Shen and X. X. Zhang, *Adv. Mater.*, 2016, **28**, 6887–6893.
30 S. L. Zuo, Y. Zhang, L. C. Peng, X. Zhao, R. Li, H. Li, J. F. Xiong, M. He, T. Y. Zhao, J. R. Sun, F. X. Hu and B. G. Shen, *Nanoscale*, 2018, **10**, 2260–2266.
31 X. Xu, W. Ito, I. Katakura, M. Tokunaga and R. Kainuma, *Scr. Mater.*, 2011, **65**, 946–949.
32 Y. Shen, R. Wang, Z. Sun, G. Cheng, Z. Xia and L. Li, *J. Mater. Sci.: Mater. Electron.*, 2014, **25**, 2030–2034.
33 R. Kainuma, K. Oikawa, W. Ito, Y. Sutou, T. Kanomata and K. Ishida, *J. Mater. Chem.*, 2008, **18**, 1837.
34 J. I. Pérez-Landazábal, V. Recarte, V. Sánchez-Alarcos, C. Gómez-Polo, S. Kustov and E. Cesari, *J. Appl. Phys.*, 2011, **109**, 093515.
35 M. K. Chattopadhyay, K. Morrison, A. Dupas, V. K. Sharma, L. S. Sharath Chandra, L. F. Cohen and S. B. Roy, *J. Appl. Phys.*, 2012, **111**, 053908.
36 D. M. Raj kumar, D. V. Sridhara Rao, N. V. Rama Rao, M. Manivel Raja, R. K. Singh and K. G. Suresh, *Intermetallics*, 2012, **25**, 126–130.
37 L. Zhou, A. Mehta, A. Giri, K. Cho and Y. Sohn, *Mater. Sci. Eng., A*, 2015, **646**, 57–65.
38 C. Phatak, O. Heinonen, M. De Graef and A. Petford-Long, *Nano Lett.*, 2016, **16**, 4141–4148.
39 H. S. Park, Y. Murakami, D. Shindo, V. A. Chernenko and T. Kanomata, *Appl. Phys. Lett.*, 2003, **83**, 3752–3754.
40 V. Recarte, J. I. Pérez-Landazábal, V. Sánchez-Alarcos and J. A. Rodríguez-Velamazán, *Acta Mater.*, 2012, **60**, 1937–1945.